Mixed convection flow of a Bingham plastic in an eccentric annulus

N. Patel and D. B. Ingham
Department of Applied Mathematical Studies, University of Leeds, Leeds LS2 9JT, England

The modeling of laminar, fully developed mixed convection flow of a Bingham plastic in a vertical eccentric annulus, in which the walls are held at asymmetric constant temperatures is investigated. The momentum, continuity and energy equations are solved numerically using the finite-element method. The results obtained are found to be in good agreement with the analytical solutions found by using a narrow gap approximation; that is, the gap between the walls of the annulus is small compared with the inner radius. It is shown that different flow configurations exist depending on the buoyancy parameter, Grashof/Reynolds, including flow reversal and unsheared plug flow adjacent to the wall. Furthermore, if flow reversal occurs it is shown by the finite-element method that a pair of "true plugs" in which the velocity is independent of both the radial and azimuthal variables can exist at each of the widest and narrowest regions of the annulus.

Keywords: mixed convection; Bingham plastic; finite-element method; narrow gap approximation

Introduction

Considerable attention has been given to the problem of forced convection flows with a non-Newtonian viscosity. However, many of these researchers have neglected the buoyancy forces, whereas the work of others has shown that for Newtonian fluids the free convection effects may be very important for surprisingly low applied temperature gradients. It is, therefore, important that the mixed convection effects of non-Newtonian flows are similarly investigated.

This area of study is of great relevance as many of the fluids used for industrial purposes are non-Newtonian. The rheology investigated here, namely, the Bingham plastic, is among the most important. In the analysis of any non-Newtonian fluid the specification of the viscous term in the Navier-Stokes equation is the most important step. The Bingham plastic differs from a Newtonian fluid in that it will either not flow or will flow as an unsheared plug below a certain yield stress. Above this critical value the relationship between the stress and the rate of strain is linear as for Newtonian fluids. Industrial applications where the mixed convection effects of Bingham plastics in eccentric annuli are encountered include the flow of drilling and cementing mud in an oil well because, throughout the life cycle of the well, temperatures of fluids in the bore-well vary and the temperature distribution in the formation changes; a detailed knowledge of the temperature distribution is vital for a correct job design and execution. One such operation is the placement of "cement" between the formation and the casing—the Bingham rheology can be experimentally shown to be representative of the cement. In this operation cement is first pumped down the well, inside the casing, and then back up the annulus displacing the drilling mud. To achieve this the setting time of the cement must be accurately controlled, the temperature being a parameter that strongly affects the setting time. The flow of molten plastics in extrusion apparatus is another of the major industrial applications where the mixed convection flow of Bingham plastics is important; other applications can be found in the review article by Bird et al. (1983).

In the present study, the assumption that the flow is fully developed, steady and laminar is made. This area of research has been extensively documented for Newtonian fluids. Tao (1960) describes an analytical method for solving the problem of fully developed mixed convection in a vertical parallel-plate duct. Further studies undertaken by Aung and Worku (1986a, 1986b) describe how asymmetric wall temperatures lead to a skewness in the velocity profile and, if the magnitude of the buoyancy parameter Grashof/Reynolds is large enough, how flow reversal can occur at the cold wall. An exact solution for the velocity distribution in the fully developed region is provided. More recent work by Ingham et al. (1988) emphasizes the occurrence of regions of flow reversal and describes a method to deal with them numerically in undeveloped flows.

The literature on the isothermal flow of Newtonian fluids in eccentric annuli is also well documented; see, for example, Snyder and Goldstein (1965) who provide an exact solution for the velocity distribution. The study of the corresponding non-Newtonian fluid flow model is, however, less well documented. Bird et al. (1983) reviewed the known exact solutions for the flow of the Bingham plastic in simple geometries including the parallel-plate duct and the concentric annulus. Guckes (1975) obtained numerical results for the Bingham plastic in an eccentric annulus over a limited parameter space, whereas Walton and Bittleston (1991) describe both analytical and numerical solutions for the isothermal flow of a Bingham plastic.

Relatively little attention has been paid to the mixed convection, non-Newtonian fluid flow model. Jones (1991) studied the mixed convection flow of the Bingham plastic in the parallel-plate duct but does not provide a quantifiable analytical solution.

The present study has been sectioned in five parts. The analysis section that follows describes the scaling and equations

Address reprint requests to Professor Ingham at the Department of Applied Mathematical Studies, University of Leeds, Leeds LS2 9JT, England.

Received 19 November 1982; accepted 18 October 1983

used throughout the article. The third section describes how a narrow gap approximation has been used to provide an analytical solution, and the penultimate section shows how a bipolar transformation can be employed to a simplified energy equation. This solution is then used in the momentum equation in its solution by the adopted numerical scheme, namely, the finite-element method (FEM). The concluding section shows the results found by using this scheme and makes a comparison between the results from the numerical and analytical solutions.

Analysis

The continuity equation for an incompressible fluid can be written as

$$\nabla^* \cdot \underline{u}^* = 0 \tag{1}$$

where asterisks denote dimensional quantities. The momentum equation can be written as

$$\rho^* \frac{D^* \underline{u}^*}{Dt^*} = -\nabla^* p^* + \rho^* \underline{g}^* - \nabla^* \cdot \underline{\tau}^* \tag{2}$$

where ρ^* is not constant everywhere.

Neglecting expansion damping and viscous dissipation the energy equation can be written

$$\frac{\partial T^*}{\partial t^*} + (\underline{u}^* \cdot \nabla^*) T^* = \tilde{\alpha} \nabla^2 T^* \tag{3}$$

We take into consideration the effect of the density gradients resulting from the temperature variations, by using the Boussinesq approximation in the gravitational or buoyancy term.

$$\rho^* = \rho_m^* (1 - \tilde{\beta}^* (T^* - T_m^*)) \tag{4}$$

Elsewhere we use $\rho^* = \rho_m^*$, where ρ_m^* is the density at a reference point taken to be at the mean of the two wall temperatures. Using this approximation the momentum equation becomes

$$\rho_m^* \frac{D^* \underline{u}^*}{Dt^*} = -\nabla^* p^* - \nabla^* \cdot \underline{\tau}^* + \rho_m^* \underline{g}^* (1 - \tilde{\beta} (T^* - T_m^*)) \tag{5}$$

The relationship between the stress tensor and rate of strain tensor is given by

$$\underline{\tau}^* = \mu^* \underline{\dot{\gamma}}^* \qquad \tau^* > \tau_y^* \tag{6}$$

where

$$\mu^* = \mu_o^* + \frac{\tau_y^*}{(\dot{\gamma}^*)} \tag{7}$$

is the Bingham rheology, and

$$\underline{\dot{\gamma}}^* = 0 \qquad \tau^* \le \tau_y^* \tag{8}$$

In the preceding, $\underline{\tau}^*$ is the stress tensor, $\underline{\dot{\gamma}}^*$ the rate of strain tensor, τ_y^* the yield stress and μ_o^* the consistency. The second invariant of the stress and rate of strain tensors are defined by

$$\tau^* = [\tfrac{1}{2}(\underline{\tau}^* : \underline{\tau}^*)]^{1/2} \qquad \dot{\gamma}^* = [\tfrac{1}{2}(\underline{\dot{\gamma}}^* : \underline{\dot{\gamma}}^*)]^{1/2} \tag{9}$$

Because the regions where the stress falls below the yield stress are unknown a priori, these have to be calculated as part of the solution.

For a fully developed steady, laminar flow the momentum equation becomes

$$\nabla^* p^* = -\nabla^* \cdot \underline{\tau}^* + \rho_m^* \underline{g}^* (1 - \tilde{\beta} (T^* - T_m^*)) \tag{10}$$

and the energy equation

$$\tilde{\alpha} \nabla^2 T^* = 0 \tag{11}$$

Using the notation shown in Figure 1 the eccentricity, e is defined to be $e^*/(R_o^* - R_i^*)$. Equations 1–11 can be non-dimensionalized using w_o^* as a velocity scale in the vertical direction and d^* as a length scale where $d^* = R_o^* - R_i^*$

$$w = \frac{w^*}{w_o^*} \qquad x = \frac{x^*}{d^*} \qquad y = \frac{y^*}{d^*} \qquad \mu = \frac{\mu^*}{\mu_o^*} \tag{12}$$

$$\underline{\tau} = \frac{\underline{\tau}^*}{\mu_o^*} \left(\frac{d^*}{w_o^*} \right) \qquad \underline{\dot{\gamma}} = \underline{\dot{\gamma}}^* \left(\frac{d^*}{w_o^*} \right) \qquad T = \frac{T^* - T_m^*}{T_o^* - T_m^*} \tag{13}$$

and the modified pressure p

$$p = \frac{d^{*2}}{\mu_o^* w_o^*} (p^* - \rho_m^* g^* z^*) \tag{14}$$

Notation

Bn	Bingham number
Gr	Grashof number
N_i	shape functions
P	pressure gradient
Re	Reynolds number
R_i^*	radius of inner cylinder
R_o^*	radius of outer cylinder
T^*	temperature of fluid
T_i^*	temperature at the cold inner cylinder
T_m^*	mean wall temperature
T_o^*	temperature at the hot outer cylinder
d^*	outer radius – inner radius
e^*	distance between axes of cylinders
g^*	acceleration due to gravity
p	modified pressure
p^*	pressure
$\hat{r}$	radial coordinate
r^*	radial distance
t^*	time
$\underline{u}^*$	velocity vector
w^*	vertical velocity
w_o^*	mean vertical velocity
z^*	axial coordinate

Greek letters

α, β	bipolar coordinates
$\tilde{\alpha}$	diffusivity
$\tilde{\beta}$	coefficient of isothermal compressibility
$\dot{\gamma}^*$	rate of strain tensor
δ	gap width
ε	small number used for numerical purposes
θ	azimuthal direction
μ_o^*	consistency
ξ, η	local coordinates used in the finite-element method
ρ^*	fluid density
ρ_m^*	fluid density at the mean temperature
τ_y^*	yield stress
$\underline{\tau}^*$	stress tensor
χ	radii ratio

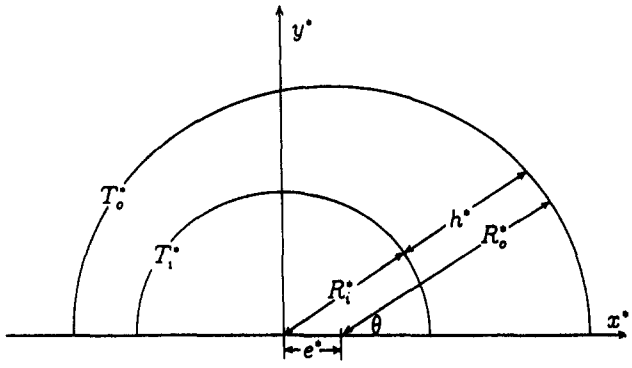

Figure 1 Schematic diagram of the eccentric annulus

The Grashof number, Gr, is given by

$$\mathrm{Gr} = \frac{\rho_m^{*2} g^* \tilde{\beta} (T_o^* - T_m^*) d^{*3}}{\mu_o^{*2}} \tag{15}$$

the Bingham number, Bn, by

$$\mathrm{Bn} = \frac{\tau_y^*}{\mu_o^*}\left(\frac{d^*}{w_o^*}\right) \tag{16}$$

and the Reynolds number, Re, by

$$\mathrm{Re} = \frac{\rho_m^* d^* w_o^*}{\mu_o^*} \tag{17}$$

The nondimensional equations are

$$\tau = \mu \dot{\gamma} \qquad \tau > \mathrm{Bn} \tag{18}$$

$$\dot{\gamma} = 0 \qquad \tau \leq \mathrm{Bn} \tag{19}$$

where

$$\mu = 1 + \frac{\mathrm{Bn}}{\dot{\gamma}} \tag{20}$$

$$-\nabla \cdot \underline{\tau} = P + \frac{\mathrm{Gr}}{\mathrm{Re}}(\mathrm{T}) \tag{21}$$

$$\nabla^2 \mathrm{T} = 0 \tag{22}$$

and $P = dp/dz$. The equation of motion is also subject to the volume flow constraint

$$\frac{\int\int w dA}{\int\int dA} = 1 \tag{23}$$

which along with the equation of motion determines P as well as the velocity field.

The relevant boundary conditions required in the preceding geometry are no slip on the vertical walls and the prescribed temperatures at the walls, namely, T_i^* on the inner cold wall and T_o^* on the outer hot wall. On nondimensionalizing these boundary conditions we find that

$$\text{on the inner cylinder } w = 0 \quad \text{and} \quad \mathrm{T} = -1 \tag{24}$$

$$\text{on the outer cylinder } w = 0 \quad \text{and} \quad \mathrm{T} = +1 \tag{25}$$

Narrow gap approximation

The assumption that the gap between the walls of the annulus is everywhere small in comparison with the inner radius is made. This can be perceived to be, to leading order, the equivalent of treating the annulus as a slot of variable width. To do this we define a dimensionless radial coordinate, $\hat{r}$ by

$$r^* = r_i^*(1 + \delta \hat{r}) \tag{26}$$

where r_i^* is the radius of the inner bounding wall, and $\delta = d^*/r_i^*$ is a dimensionless gap width. We note that the bounding walls can now be represented by $\hat{r} = 0$ and $\hat{r} = h(\theta)$, where θ and $h = h^*/d^*$ are shown in Figure 1 and can be defined by the equation

$$(e^2 + h^2 - 2eh\cos\theta - 1)\delta = 2(1 + e\cos\theta - h) \tag{27}$$

Effectively the narrow gap approximation requires $\delta \to 0$ while the eccentricity remains $O(1)$. We thus expand h in powers of δ

$$h = h_o + \delta h_1 + O(\delta^2) \tag{28}$$

and observe that

$$h_o = 1 + e\cos\theta \tag{29}$$

In terms of the new coordinates $(\hat{r}, \theta, z)$ Equation 21 becomes

$$\frac{\partial \tau_{\hat{r}z}}{\partial \hat{r}} + \frac{\delta}{1 + \delta\hat{r}}\left(\tau_{\hat{r}z} + \frac{\partial \tau_{\theta z}}{\partial \theta}\right) = -P - \frac{\mathrm{Gr}}{\mathrm{Re}}(\mathrm{T}) \tag{30}$$

For this model, we have

$$\dot{\gamma}_{\hat{r}z} = \frac{\partial w}{\partial \hat{r}} \tag{31}$$

$$\dot{\gamma}_{\theta z} = \frac{\delta}{1 + \delta\hat{r}}\left(\frac{\partial w}{\partial \theta}\right) \tag{32}$$

and expanding w as

$$w = w_o + \delta w_1 + O(\delta^2) \tag{33}$$

we have

$$\tau_{\hat{r}z} = \mu \dot{\gamma}_{\hat{r}z} = \mu \frac{\partial w_o}{\partial \hat{r}} + O(\delta) \tag{34}$$

$$\tau_{\theta z} = \mu \dot{\gamma}_{\theta z} = O(\delta) \tag{35}$$

The energy equation (Equation 22) therefore becomes

$$\frac{\partial^2 \mathrm{T}}{\partial \hat{r}^2} + \frac{\delta}{1 + \delta\hat{r}}\left(\frac{\partial \mathrm{T}}{\partial \hat{r}}\right) + \frac{\delta^2}{[1 + \delta\hat{r}]^2}\left(\frac{\partial^2 \mathrm{T}}{\partial \theta^2}\right) = 0 \tag{36}$$

By expanding T as

$$\mathrm{T} = \mathrm{T}_o + \delta \mathrm{T}_1 + O(\delta^2) \tag{37}$$

and equating leading order of powers of δ, we have

$$\frac{\partial^2 \mathrm{T}}{\partial \hat{r}^2} = 0 \tag{38}$$

which implies that

$$\mathrm{T}_o = A\hat{r} + B \tag{39}$$

Imposing the boundary conditions on

$$\hat{r} = 0, \quad \mathrm{T} = -1 \quad \text{and on } \hat{r} = h_o, \quad \mathrm{T} = +1 \tag{40}$$

we have

$$\mathrm{T}_o = \left(\frac{2}{h_o}\right)\hat{r} - 1 \tag{41}$$

where h_o is given by Equation 29. Thus the leading terms

in Equation 30 give

$$\frac{\partial \tau_{\hat{t}z}}{\partial \hat{r}} = -P - \frac{Gr}{Re}\left[\left(\frac{2}{h_o}\right)\hat{r} - 1\right] \tag{42}$$

It is now convenient to note that the analytical solution for this mixed convection model is more complex than the corresponding isothermal case. In the latter model, one could appeal to the symmetry in the radial direction, whereas this is no longer the situation. Additionally, whereas only one fundamental flow configuration of interest exists in the isothermal model, essentially there are now four as shown in Figure 2. The first configuration is shown schematically in Figure 2a. At the hot outer wall (*right*) the buoyancy force acts vertically upward, with a corresponding buoyancy force acting vertically downward adjacent to the cold wall. When the Grashof number is small, as in this configuration, the vertically upward acting pressure gradient is not great enough to overcome the buoyancy effect at the cold wall, and no reverse flow or zero velocity flow occurs. As the Grashof number increases, the buoyancy effects are increased. A situation is reached where the buoyancy force now overcomes the pressure gradient adjacent to the cold wall, to an extent where the stress is less than the yield stress and hence zero velocities occur as shown schematically in Figure 2b. In Figure 2c, the buoyancy force exceeds the pressure gradient at the cold left wall to such an extent that the yield stress is overcome here. At the hot right wall the combination of the pressure gradient and buoyancy forces are unable to overcome the yield stress. Finally, increasing the Grashof number further results in a reverse flow situation as shown schematically in Figure 2d. From Equations 20 and 34 we have, to leading order,

$$\tau_{\hat{t}z} = \frac{\partial w_o}{\partial \hat{r}} + \mathrm{Bn}\ sgn\left(\frac{\partial w_o}{\partial \hat{r}}\right) \tag{43}$$

The analytical solution for Equation 42 therefore requires previous knowledge about the directions of the velocity gradient. It is therefore necessary to consider each profile and region separately. For the purposes of this study, results are

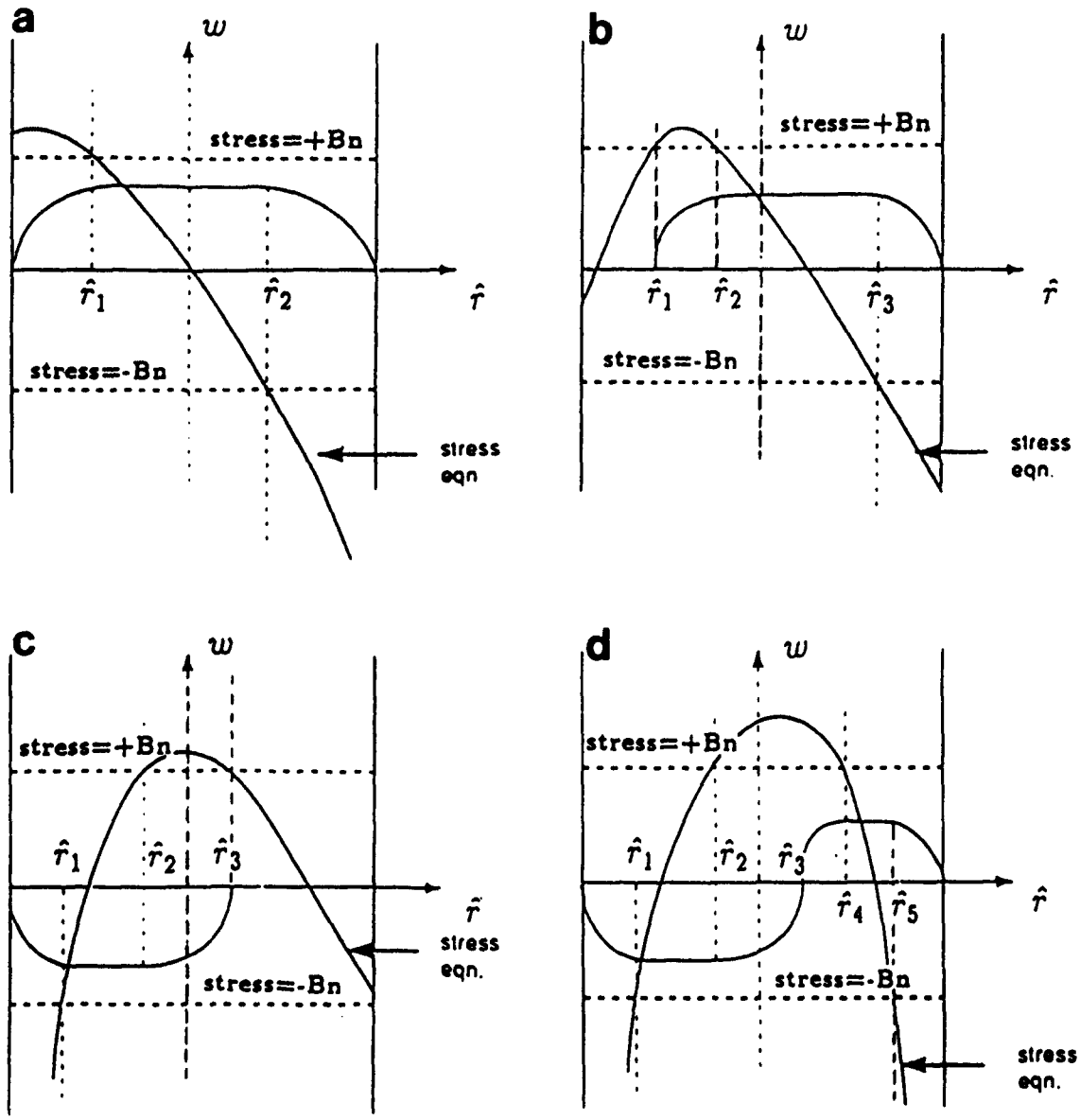

Figure 2 The four possible velocity profiles for Bingham plastics with superimposed schematic stress fields

only shown for the profile corresponding to Figure 2a, but results for the remaining three profiles have been found using similar techniques. The flow through the duct with respect to Figure 2a is given by

$$0 \le \hat{r} \le \hat{r}_1$$

$$w_o = -\left(P - \frac{Gr}{Re}\right)\frac{\hat{r}^2}{2} - \frac{Gr}{Re}\frac{\hat{r}^3}{3h_o} - (Bn - k)\hat{r} \tag{44}$$

$$\hat{r}_1 \le \hat{r} \le \hat{r}_2$$

$$w_o = w_{plug} \tag{45}$$

$$\hat{r}_2 \le \hat{r} \le h_0$$

$$w_o = -\frac{1}{2}\left(P - \frac{Gr}{Re}\right)(\hat{r}^2 - h_o^2) - \frac{1}{3h_o}\frac{Gr}{Re} \times (\hat{r}^3 - h_o^3) + Bn(\hat{r} - h_o) + k(\hat{r} - h_o) \tag{46}$$

where w_{plug} is given by

$$w_{plug} = -\left(P - \frac{Gr}{Re}\right)\frac{\hat{r}_1^2}{2} - \frac{Gr}{Re}\frac{\hat{r}_1^3}{3h_o} - (Bn - k)\hat{r}_1 \tag{47}$$

$$= -\frac{1}{2}\left(P - \frac{Gr}{Re}\right)(\hat{r}_2^2 - h_o^2) - \frac{1}{3h_o}\frac{Gr}{Re} \times (\hat{r}_2^3 - h_o^3) + Bn(\hat{r}_2 - h_o) + k(\hat{r}_2 - h_o) \tag{48}$$

We see from the preceding that the velocity profiles contain an unknown constant of integration k. To overcome this difficulty the equations for the plug flows are considered. These occur in pairs and include the desired constant, other known parameters and the yield points (the $\hat{r}_p$'s in Figure 2 where $p = 1, 2, \ldots 5$). The yield points can themselves be written in terms of the constant of integration by noting that the stress has to be equal to $\pm$Bn at these points. Applying this condition to the leading order stress Equation 42 we find that

$$\hat{r}_p^+ = \frac{-\left(P - \frac{Gr}{Re}\right) \pm \left[\left(P - \frac{Gr}{Re}\right)^2 + 4\left(\frac{Gr}{h_o Re}\right)(Bn + k)\right]^{1/2}}{\frac{2Gr}{h_o Re}} \tag{49}$$

$$\hat{r}_p^- = \frac{-\left(P - \frac{Gr}{Re}\right) \pm \left[\left(P - \frac{Gr}{Re}\right)^2 - 4\left(\frac{Gr}{h_o Re}\right)(Bn - k)\right]^{1/2}}{\frac{2Gr}{h_o Re}} \tag{50}$$

where $\hat{r}_p^+$ are the values of $\hat{r}$ when the stress equals $+$Bn and $\hat{r}_p^-$ the corresponding values of $\hat{r}$ when the stress equals $-$Bn (see Figure 2 for schematically superimposed stress fields). We have for this profile

$$-\frac{1}{2}\left(P - \frac{Gr}{Re}\right)(\hat{r}_1^2 - \hat{r}_2^2 + h_o^2) - \frac{1}{3h_o}\frac{Gr}{Re}(\hat{r}_1^3 - \hat{r}_2^3 + h_o^3) - Bn(\hat{r}_1 + \hat{r}_2 - h_o) + k(\hat{r}_1 - \hat{r}_2 + h_o) = 0 \tag{51}$$

The solution to this equation and the corresponding equations for the profiles as shown in Figures 2b–d can be found numerically using Brent's method which combines bisection and inverse quadratic interpolation and is described in Press et al. (1990). Figure 2a shows a positive velocity gradient at the inner wall implying a stress greater than $+$Bn (see Equation 43). Similarly, the stress at the hot outer wall has a value less than $-$Bn owing to the negative velocity gradient. Arguments of a similar nature are applied to the remaining profiles. When these conditions are inserted in the stress equation (Equation 42) the following results, which refer to Figures 2a–d, respectively are obtained:

$$Ph_o - Bn > k > Bn \tag{52}$$

$$\min(Ph_o - Bn, Bn) > k > -Bn \tag{53}$$

$$\min(Ph_o + Bn, -Bn) > k > -Bn + Ph_o \tag{54}$$

$$\min(Ph_o - Bn, -Bn) > k \tag{55}$$

The constant of integration k can only be satisfied by any one of the four fundamental sets of inequalities given earlier, for any given combination of P, h_o and the Bingham number, Bn.

The analytical solution therefore involves sweeping anticlockwise from $\theta = 0$ to $\theta = \pi$ finding the radial profile at each θ for a given pressure gradient. When a constant flow rate is specified, the pressure is iterated on until the correct flow rate is found.

Numerical solution

Numerical solutions for this mixed convection model have been found by employing the FEM. One of the major problems encountered when using the Bingham plastic rheology is the theoretically infinite viscosity in regions of plug flow. Finite difference methods are particularly susceptible and encounter convergence difficulties through loss of significant digits. The FEM has the advantage over this and other methods in that it can be extended to higher dimension problems, to more complex geometries and, most important, remain stable in the regions of plug flow. However, it is still necessary to introduce a small parameter, ε into the rheology to avoid the possibility of a singularity when the shear rate γ^* becomes identically zero (i.e., when the yield surface is approached). The approach is the one adopted by numerous authors including Beris et al. (1985). The only occurrence of the method being previously used with non-Newtonian fluids of any kind in an eccentric annulus is by Walton and Bittleston (1991) to find the solution for the isothermal axial flow of a Bingham plastic.

With reference to Equations 20–22 we have the viscosity, momentum and energy equations.

$$\mu = 1 + \frac{Bn}{(\dot{\gamma}) + \varepsilon} \tag{56}$$

$$-\frac{\partial \tau_{xz}}{\partial x} - \frac{\partial \tau_{yz}}{\partial y} = P + \frac{Gr}{Re}(T) \tag{57}$$

$$\nabla^2 T = 0 \tag{58}$$

For the solution to the energy equation (Equation 58) in the eccentric annulus, a bipolar transformation is used. The bipolar coordinates are defined by the transformation

$$x + iy = ic\cot\left(\frac{\alpha + i\beta}{2}\right) \tag{59}$$

where c is a constant. In accordance with the work of Snyder and Goldstein (1965) we have

$$x = \frac{c\sinh\beta}{\cosh\beta - \cos\alpha} \tag{60}$$

$$y = \frac{c\sin\alpha}{\cosh\beta - \cos\alpha} \tag{61}$$

where $0 \leq \alpha \leq 2\pi$, and $-\infty < \beta < +\infty$. Because of the symmetry of the problem, it is again only necessary to consider half of the annulus. The transformation from physical to bipolar coordinates maps the eccentric annulus to the rectangular region shown in Figure 3.

The Laplacian of the temperature, T, in bipolar coordinates is

$$\nabla^2 T = \frac{(\cosh\beta - \cos\alpha)^2}{c^2}\left(\frac{\partial^2 T}{\partial\alpha^2} + \frac{\partial^2 T}{\partial\beta^2}\right) + \frac{\partial^2 T}{\partial z^2} \tag{62}$$

For this fully developed model, the temperature variation is only dependent on β, that is, the energy equation is reduced to

$$\frac{\partial^2 T}{\partial\beta^2} = 0 \tag{63}$$

for which the solution in bipolar coordinates is found to be

$$T = \frac{\beta_o + \beta_i - 2\beta}{\beta_i - \beta_o} \tag{64}$$

where β_i is the value of β on the inner cylinder and β_o the value on the outer cylinder. It can be shown that

$$c = R_o^* \sinh\beta_o = R_i^* \sinh\beta_i \tag{65}$$

$$\beta_i = \cosh^{-1}\left[\frac{\chi(1+e^2)+(1-e^2)}{2\chi e}\right] \tag{66}$$

$$\beta_o = \cosh^{-1}\left[\frac{\chi(1-e^2)+(1+e^2)}{2e}\right] \tag{67}$$

where $\chi = R_i^*/R_o^*$ and e is the eccentricity. Inverse hyperbolic cosine functions cannot be evaluated by computational methods, consequently Equations 66 and 67 are transformed to logarithmic functions, that is,

$$\beta_i = \ln(A + (A^2 - 1)^{1/2}) \tag{68}$$

where

$$A = \frac{\chi(1+e^2)+(1-e^2)}{2\chi e} > 1 \tag{69}$$

and

$$\beta_0 = \ln(B + (B^2 - 1)^{1/2}) \tag{70}$$

where

$$B = \frac{\chi(1-e^2)+(1+e^2)}{2e} > 1 \tag{71}$$

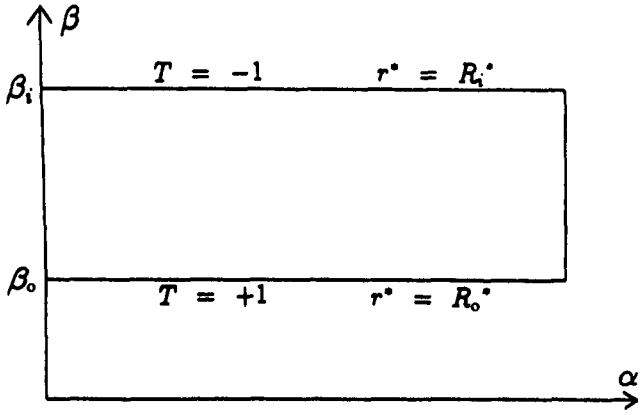

Figure 3 The geometry in the transformed bipolar plane

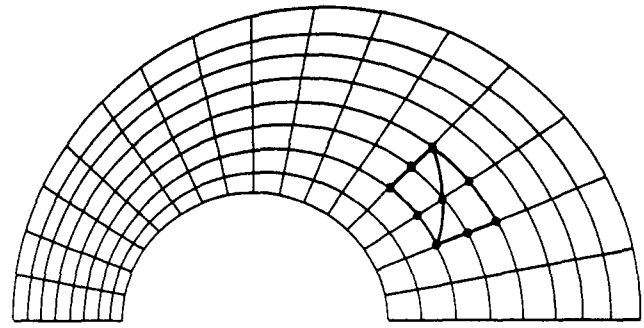

Figure 4 Schematic diagram showing the mesh

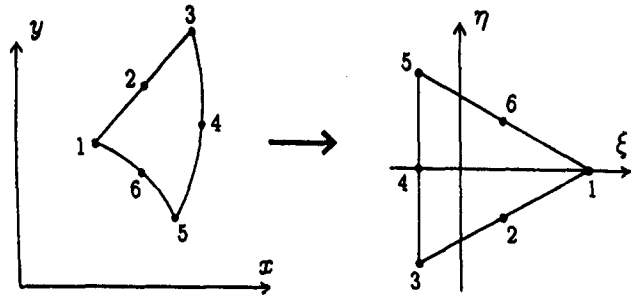

Figure 5 The parametric element mapping

The final equation necessary to transform Equation 64 back to the Cartesian coordinate system is

$$\beta = \frac{1}{2}\ln\left[\frac{y^2 + (x+c)^2}{y^2 + (x-c)^2}\right] \tag{72}$$

A solution for the energy equation can therefore be found analytically in the required coordinates.

The finite element method was applied using six-noded triangular elements, where an iso-parametric transformation allows the elements to align themselves with the boundary. The mesh is shown in Figure 4.

The curvilinear element in the x-y plane is mapped onto a triangle in the $\xi - \eta$ plane as shown in Figure 5. The (x_i, y_i) points are the nodal positions in the x-y plane, so we can write

$$x = \sum_{i=1}^{6} N_i(\xi, \eta) x_i \tag{73}$$

$$y = \sum_{i=1}^{6} N_i(\xi, \eta) y_i \tag{74}$$

where N_i are the shape functions. In terms of the local area coordinates these are, for a typical corner node,

$$N_3 = (2L_2 - 1)L_2 \tag{75}$$

and for the typical mid-side node,

$$N_4 = 4L_2L_3 \tag{76}$$

where L_1, L_2 and L_3 are the area coordinates associated with the three vertices of the standard triangle. In terms of the local Cartesian coordinate system we have

$$L_1(\xi, \eta) = \tfrac{1}{3}(1 + 2\xi) \tag{77}$$

$$L_2(\xi, \eta) = \tfrac{1}{3}(1 - \xi - \sqrt{3}\eta) \tag{78}$$

$$L_3(\xi, \eta) = \tfrac{1}{3}(1 - \xi + \sqrt{3}\eta) \tag{79}$$

The solution w may be approximated by

$$w = \sum_{i=1}^{6} N_i(\xi, \eta) w_i \tag{80}$$

where w_i are the nodal values of the velocity.

Defining the inner product to be

$$\langle l; m \rangle = \iint_A lm \, dA \tag{81}$$

we obtain for each element

$$\langle N_i; -\nabla \cdot (\mu \nabla w) \rangle = \left\langle N_i; P + \frac{Gr}{Re}(T) \right\rangle \tag{82}$$

where T is found using Equations 64–72. Using Green's theorem and ignoring the boundary integrals that cancel on the element to element boundaries we obtain

$$\langle N_{i,x}; \mu w_x \rangle + \langle N_{i,y}; \mu w_y \rangle = P\langle N_i; 1 \rangle + \frac{Gr}{Re} \langle N_i; T \rangle \tag{83}$$

where $N_{i,x}$ equals $\partial N_i / \partial x$. As this equation cannot be integrated directly, solutions were produced using a seven-point Gaussian quadrature rule for each element. It is also necessary to find the rate of strain over each element so that the viscosity variation can be found. Using Equation 80 we can show that

$$\dot{\gamma} = \left[\left(\sum_{i=1}^{6} N_{i,x} w_i \right)^2 + \left(\sum_{i=1}^{6} N_{i,y} w_i \right)^2 \right]^{1/2} \tag{84}$$

Noting that μ is a function of the velocity, and consequently Equation 83 forms a nonlinear system of equations, we use Picard iteration to linearize the system thereby removing this difficulty. The method of Walton and Bittleston (1991) can be used to find the pressure gradient, P, by writing the volume flow constraint, Equation 23 as

$$\langle w; 1 \rangle = \langle 1; 1 \rangle \tag{85}$$

that is,

$$\sum_{i=1}^{6} \langle N_i; 1 \rangle w_i = \langle 1; 1 \rangle \tag{86}$$

The solution is found by including this equation with the equation of motion and solving for

$$(w_1, \ldots, w_n | P)^T \tag{87}$$

where there are n nodes.

Results and discussion

In the present study the main parameters are the buoyancy parameter Grashof/Reynolds, the Bingham number and the eccentricity. Although results have been produced for a wide parameter range, results are only shown for a Bingham plastic with Bingham number = 12. These results have been restricted to those where the constant volume constraint, as described by Equation 23, has been applied, and the pressure gradient, P, is therefore determined as a consequence. All the results presented in this study were calculated on a grid consisting of 25 x 41 nodal points in the radial and azimuthal directions, respectively. A comparison between these results and the corresponding ones computed on the grids involving 13 x 21 nodes and 7 x 11 nodes would suggest that the solutions obtained with the finer grid are within the required accuracy, as the solutions found using the coarser grids were within 1 and 5 percent, respectively, of those found using the finer grid. We can therefore conclude that it is unnecessary to increase the number of nodal points further and that the results have converged.

Figure 6 shows the velocity contours and the radial flow profiles found using the FEM, in the narrowest and widest sections of the annulus with the parameter Grashof/Reynolds = 250. Figure 6a represents the flow profile for a concentric annulus (eccentricity = 0). We note the presence of the expected plug in the radial direction and the tendency of the fluid to move quicker adjacent to the hot outer wall. When the eccentricity is increased to 0.25 there is a large increase in the maximum velocity in the wider section of the annulus, with a corresponding decrease in the narrower side of the annulus (see Figure 6b). A further increase in the eccentricity leads to the situation shown in Figure 6c. Here the velocity has again increased in the widest section but has almost decreased to zero in the narrow region. A careful examination reveals that this is an example of zero velocity adjacent to the cold wall. A further increase in the eccentricity would lead to zero velocity in the narrow region.

Figure 7 shows the velocity contours and profiles with the same parameters as in Figure 6, with the exception of the buoyancy parameter Grashof/Reynolds, which is increased to 500. As the eccentricity is increased the maximum and minimum velocities in the wider part of the annulus increase with a decrease in the narrower part. In Figure 7c we encounter the special case of zero flow adjacent to the hot wall with flow reversal adjacent to the cold wall in the narrower part of the annulus.

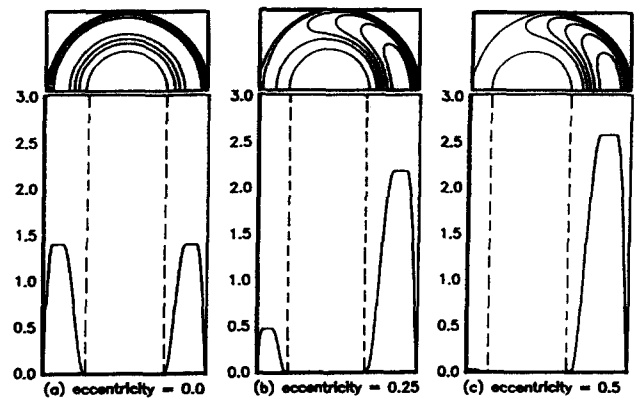

Figure 6 Velocity distribution for a Bingham plastic at Gr/Re = 250

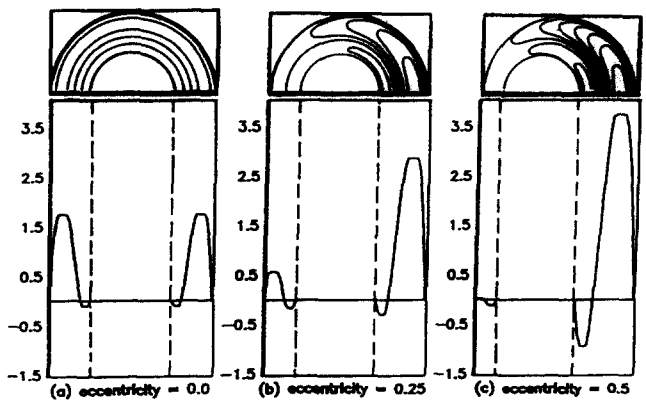

Figure 7 Velocity distribution for a Bingham plastic at Gr/Re = 500

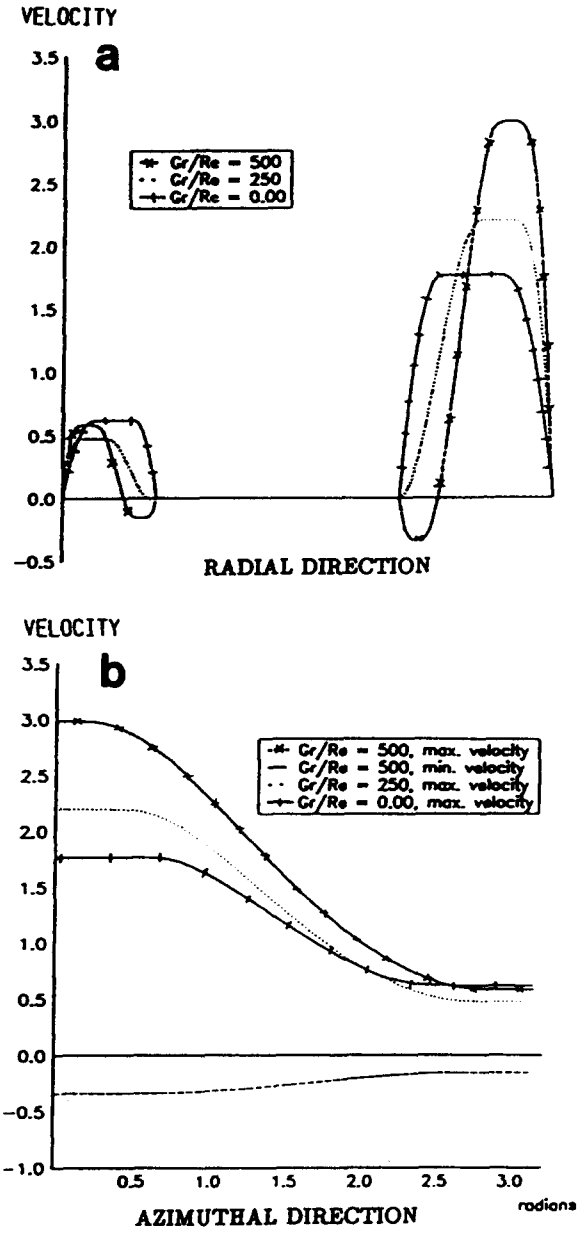

Figure 8 Radial and azimuthal velocity distributions

Figure 8a shows the numerical radial velocity profiles in the widest region of the annulus with varying buoyancy parameter Grashof/Reynolds and eccentricity = 0.25. In the study by Walton and Bittleston (1991) it is shown that there exists two types of plug in the eccentric annulus for isothermal flow. The first, referred to as a pseudoplug, occurs in the radial direction (i.e., the velocity is independent of the radial variable), whereas in the second, the velocity is also independent of the azimuthal direction. This second plug, known as a true plug, occurs at the widest, and in some cases, narrowest part of the annulus. The corresponding results for this mixed convection model are shown in Figure 8b, again plotted for a Bingham plastic, Bn = 12. The maximum velocities, found along radial lines, are plotted against the corresponding azimuthal positions when the Grashof/Reynolds number = 0, 250 and 500. When reverse flow regions exist (i.e., Gr/Re = 500), the minimum velocities are also plotted. The figure shows that true plugs can exist at the widest and narrowest part of the annulus. Furthermore, if reverse flow occurs we find two true plugs in each region provided that the flow extends azimuthally all the way around the annulus.

The results in this article have been produced by solving the momentum and energy equations (Equations 21 and 22) subject to the relevant boundary conditions. Two approaches have been used: the first, using the FEM, incorporates a bipolar transformation used to solve the simplified energy equation resulting in a nonlinear temperature gradient, and the second approach uses a narrow gap approximation giving a linear temperature gradient as shown in Figure 9.

Excellent agreement is reached (within 10 percent) when $\delta \leq 0.1$ even when the parameter Grashof/Reynolds is as high as 3,000. This is demonstrated in Figures 10a–d, which show the maximum velocities found along radial lines and plotted against corresponding azimuthal positions for parameters $\delta = 0.1$, Gr/Re = 3,000, Bn = 12 and eccentricities 0, 0.25, 0.5, and 0.75, respectively.

When the value of δ is increased to as high as 0.4, agreement between the results found by the numerical method and the narrow gap approximation is still within 20 percent provided that Grashof/Reynolds $\leq$ 500. Alternatively, if this latter parameter is increased while sustaining a high δ, the velocities remain in good agreement, although the pressure gradient, P, becomes unreliable. This is demonstrated in Table 1 in which $\delta = 0.3$, eccentricity = 0, 0.25 and 0.5 and Gr/Re = 0, 500, 1,000 and 3,000.

Figure 11a shows the nondimensional velocity plotted against the radial position in the widest region of the annulus for $\delta = 0.3$, eccentricity = 0.25 and Gr/Re = 3,000. Figure 11b shows the maximum and minimum nondimensional velocities found along radial lines and plotted against the corresponding azimuthal position for the same parameter values. Both figures clearly demonstrate the good agreement between the numerical and analytical approximation velocities. In contrast, Table 1 shows that for the corresponding parameter values the pressure gradient obtained analytically is 7, whereas the numerically predicted value is 216. By solving analytically for the Newtonian flow using quadratic polynomials to approximate for the nonlinear temperature gradient, we can show that the pressure gradient is prone to error, whereas the velocity distribution is not.

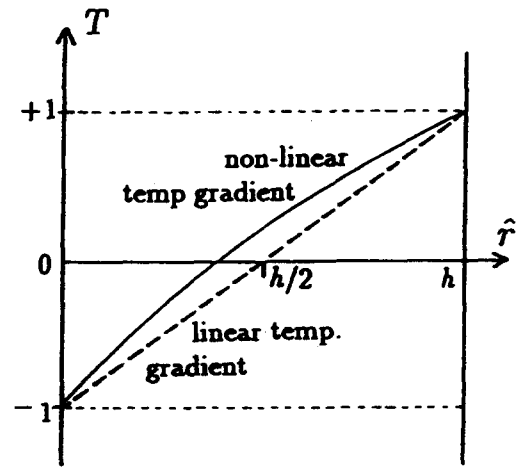

Figure 9 Temperature gradients measured in the radial direction

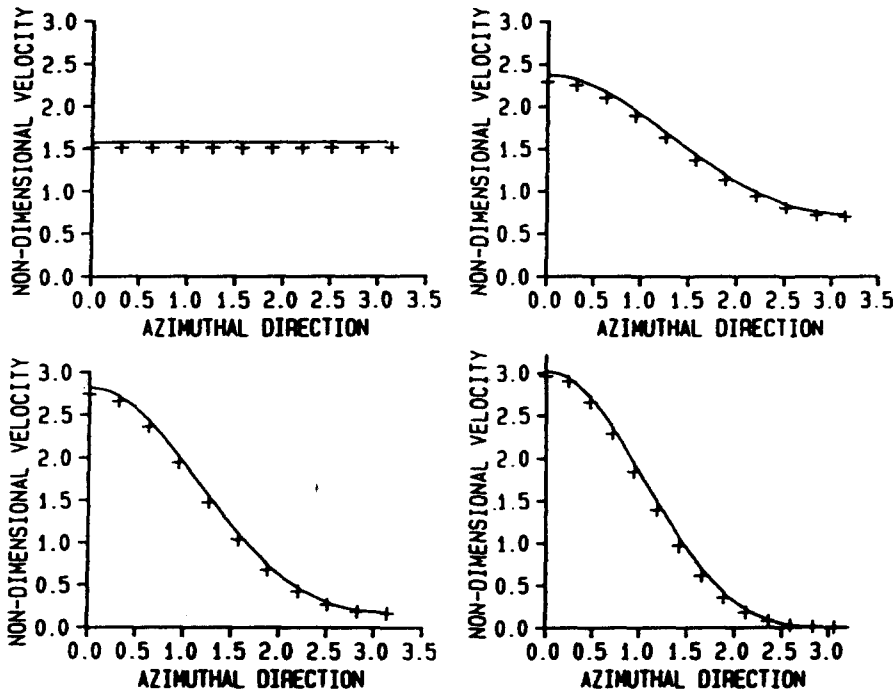

Figure 10 Maximum velocities: −analytical; + numerical

Table 1 Variation of pressure gradient obtained numerically and analytically as a function of eccentricity for Gr/Re = 0, 500, 1,000 and 3,000 and $\delta = 0.3$

	Gr/Re = 0			Gr/Re = 500		
	Pressure gradient			Pressure gradient		
$\delta = 0.3$ Eccentricity	Numerical	Analytical	Error percent	Numerical	Analytical	Error percent
0.00	379	388	2	334	378	13
0.25	349	356	2	303	345	14
0.50	288	295	2	233	274	18
Eccentricity	Gr/Re = 1,000			Gr/Re = 3,000		
0.00	284	362	27	40	246	515
0.25	247	325	32	7	216	2986
0.50	155	237	53	−86	154	—

Conclusions

Results obtained using the FEM have been compared with an approximate analytical solution that has been found by using a leading order narrow gap approximation. It is shown that four possible flow configurations exist, depending on the buoyancy parameter Grashof/Reynolds. In contrast to the corresponding isothermal model, flow reversal and motionless regions can occur adjacent to the walls of the annulus. In agreement with the findings of Walton and Bittleston (1991) plug regions exist where the velocity is constant in the radial direction. These regions, referred to as pseudoplugs, are no longer of uniform width or centrally placed as in the isothermal model, but lie adjacent to the outer wall. In flow reversal situations we find in coexistence a corresponding pseudoplug region, extending azimuthally around the annulus adjacent to the cold inner wall, with a negative plug velocity. As in the isothermal case, a motionless region filling the gap between the walls can still occur in the narrowest part of the annulus. Additionally, true plugs are identified by the FEM in the widest and narrowest regions of the annulus. It is important to note that the leading order narrow gap approximation is inadequate to predict these regions and that greater accuracy, as shown by Walton and Bittleston (1991), is required. In cases of flow reversal the possibility of a pair of true plugs, one with a constant positive velocity and the other with constant negative velocity, arises in each of the widest and narrowest parts of the annulus.

A comparison of the numerical and narrow gap approximation results shows good quantitative agreement for relatively

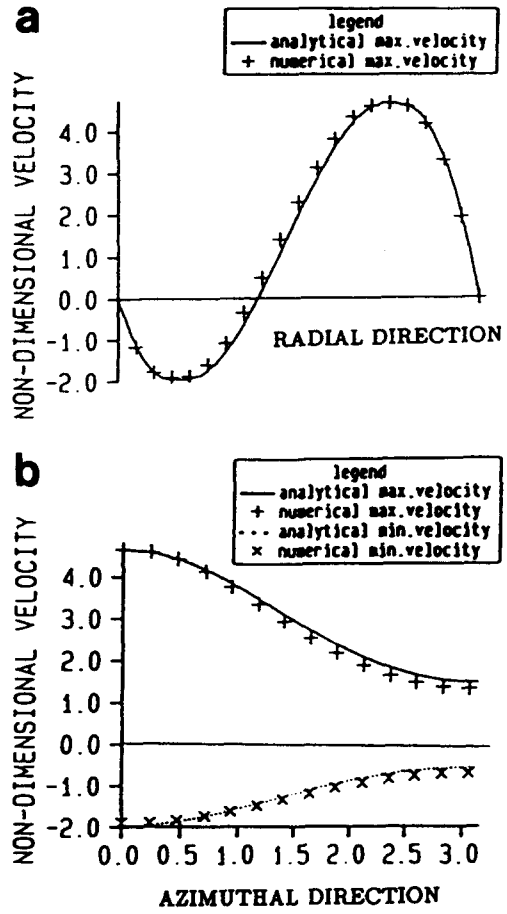

Figure 11 $\delta = 0.3$, Gr/Re = 3,000, $e = 0.25$: (a) radial velocity distribution in the widest region of the annulus; (b) variation of the maximum and minimum velocities found along radial lines and plotted against the azimuthal position

small dimensionless gap widths, δ, even when the buoyancy parameter Grashof/Reynolds is relatively high. An increase in δ still allows good agreement provided that the buoyancy parameter is relatively low. It can be shown that as this latter parameter increases, although the velocities remain in good agreement, the pressure gradient as obtained analytically deteriorates. This is primarily because of the temperature gradient approximation in the narrow gap solution.

Acknowledgment

The authors would like to thank Schlumberger Cambridge Research for their valuable support and financial assistance of this research.

References

Aung, W. and Worku, G. 1986a. Developing flow and flow reversal in a vertical channel with asymmetric wall temperatures. *ASME J. Heat Transfer*, **108**, 299–304

Aung, W. and Worku, G. 1986b. Theory of fully developed combined convection including flow reversal. *ASME J. Heat Transfer*, **108**, 485–488

Beris, A. N., Tsamopoulos, J. A., Armstrong, R. C. and Brown, R. A. 1985. Creeping motion of a sphere through a Bingham plastic. *J. Fluid Mech.*, **158**, 219–244

Bird, R. B., Dai, G. C. and Yarusso, B. J. 1983. The rheology and flow of viscoplastic materials. *Rev. Chem. Eng.*, **1**, 36–69

Guckes, T. L. 1975. Laminar flow of a non-Newtonian fluid in an eccentric annulus. *Trans. ASME J. Eng. Ind.*, **97**, 498–506

Ingham, D. B., Keen, D. J. and Heggs, P. J. 1988. Flows in vertical channels with asymmetric wall temperatures and including situations where reversal flows occur. *ASME J. Heat Transfer*, **110**, 910–917

Jones, A. T. 1991. Combined convection in vertical ducts, Ph.D. thesis, Department of Applied Mathematical Studies, University of Leeds, Leeds, England

Press, W. H., Flannery, B. P., Teukolsky, S. A. and Vetterling, W. T. 1990. *Numerical Recipes—The Art of Scientific Computing.* Cambridge University Press, New York

Snyder, W. T. and Goldstein, G. A. 1965. An analysis of fully developed flow in an eccentric annulus. *AIChE J.*, **11**, 462–467

Tao, L. N. 1960. On combined free and forced convection in channels. *ASME J. Heat Transfer*, **82**, 233–238

Walton, I. C. and Bittleston, S. H. 1991. The axial flow of a Bingham plastic in a narrow eccentric annulus. *J. Fluid Mech.*, **222**, 39–60